Steering Rotating Magnetic Swimmers in 2.5 Dimensions using only 2D Ultrasonography for Position Sensing

Yitong Lu, Haoran Zhao, Aaron T. Becker, and Julien Leclerc*

Abstract—Micro/millimeter-scale magnetic robots have many potential biomedical applications. However, there are major challenges in using these devices for *in vivo* tasks due to limitations of imaging technology for real-time detection and navigation inside the human body. Ultrasound is a popular sensor for localizing such robots because it is easy to use and less expensive than other imaging methods. This paper studies methods to track and control a millimeter-scale rotating magnetic swimmer to perform path following. Detection using ultrasound B-mode and Doppler mode to track the robot during navigation are compared. In addition, an algorithm to perform 2.5D closed-loop control (controlling 3 degrees of freedom for a swimmer to follow a planar path) of the swimmer using only 2D ultrasound feedback was studied and tested experimentally.

I. Introduction

Magnetic manipulation is a technology that enables the tetherless control of miniature objects. A robotic system monitors and controls the agents by producing a time-varying magnetic field. These tools could be helpful to perform minimally invasive surgeries. The human body is transparent to low-frequency magnetic fields. Therefore, a magnetic agent can be actuated inside a patient while the magnets generating the field are external [I]. Magnetic micro/millimeter-robots are untethered mesoscale machines that contain a magnetic material. Research groups have studied many types of these robots and showed that they could be easily controlled by external magnetic fields [2]—[6]. They are able to navigate in a controlled manner in various physiological environments [7], [8], clear *ex vivo* blood clots [9], and deliver targeted therapy [10].

Our study focuses on the control of millimeter-scale spiral-type magnetic swimmers (see Fig. []). This type of swimmer contains a permanent magnet that has a radial magnetization. The magnetic manipulator generates a rotating field that creates a torque on the swimmer and makes it rotate. The spiral shape of the swimmer produces a propulsive force. These swimmers naturally orient their main axis with the axis of

Manuscript received September 9, 2021; accepted January 5, 2022. Date of publication January 27, 2022.

This letter was recommended for publication by Associate Editor K. Rabenorosoa and Editor J. Burgner-Kahrs upon evaluation of the reviewers' comments.

This work was supported by the National Science Foundation under Grants No. [IIS-1553063] and [CNS-1932572]

Authors are with the Department of Electrical and Computer Engineering, University of Houston, Houston, TX 77204. *Corresponding author. Email: ileclerc@central.uh.edu

Digital Object Identifier (DOI): see top of this page.

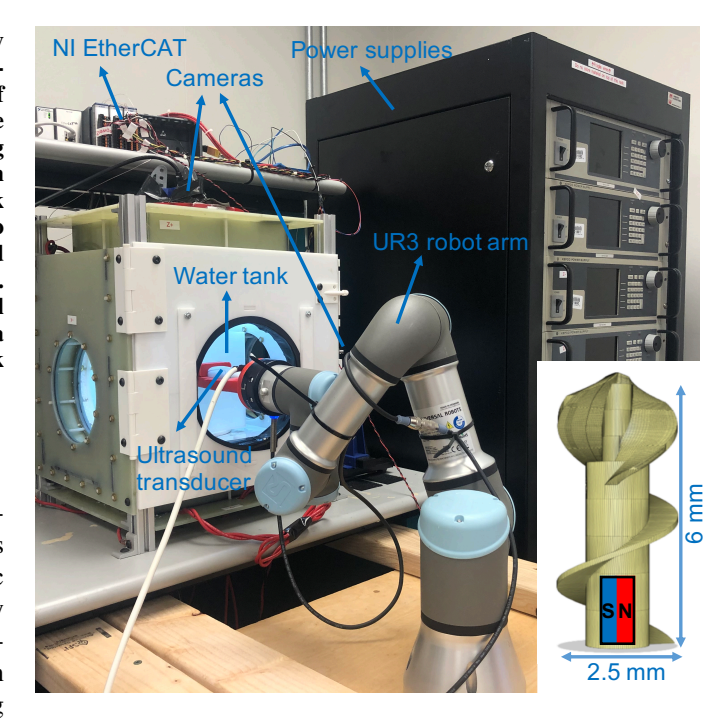


Fig. 1. Annotated photo of the robotic magnetic manipulator used in this study. In this study the robot arm statically holds the ultrasound probe. Inset: 3D CAD drawing of a spiral-type swimmer and embedded magnet.

rotation of the field. As a result, they can be steered by changing the orientation of the magnetic field rotation axis. Our previous work shows that a rotating magnetic swimmer can follow a 3D path with camera feedback [11] and remove an ex vivo blood clot [12]. Also, adding properly-sized capacitors in series with the electromagnets increases the maximum current at the operating frequency which results in an increased flux density and torque. Using capacitors enabled a maximum blood clot removal rate of 44 mm³/min [13]. Appropriatelysized spiral-type swimmers could be inserted inside a blood vessel and controlled to swim toward an area to treat. The swimmer used in this study has a diameter of 2.5 mm, which is much smaller than the size of the aorta or the pulmonary arteries. For a swimmer forward velocity of 30 to 60 mm/s, this size corresponds to a Reynolds number in the range [10, 100].

A barrier to performing closed-loop control of magnetic swimmers *in vivo* is performing the real-time imaging and tracking of these devices [14]. A variety of technologies have been explored for localizing magnetic agents. These include ultrasound (US) imaging, fluorescent imaging (FI), magnetic

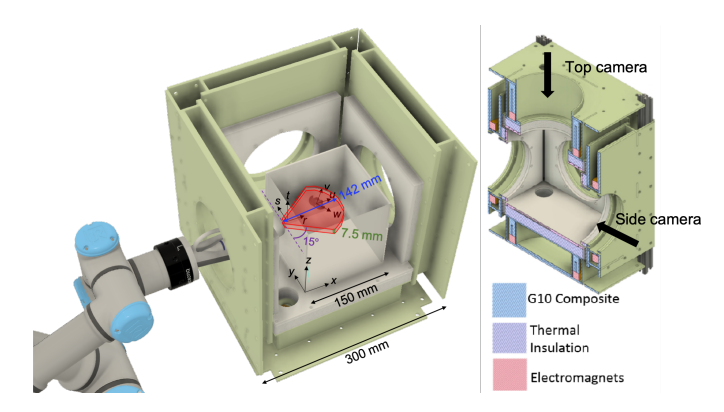


Fig. 2. Schematic showing the swimmer (scaled in size by 6x) in the workspace with the ultrasound field of view (left), and cross section of CAD drawing of the magnetic manipulator showing the electromagnets (right). Black arrows indicate the position of two cameras.

resonance imaging (MRI), and computed tomography (CT). Many researchers selected ultrasound imaging to navigate the robot [15]—[19] and for tracking the robot to remove blood clots [20], [21]. Ultrasound is a popular choice for researchers to test their systems for multiple reasons. For example, FI only enables the imaging of vessels close to the surface of a tissue and is therefore unsuitable to visualize vessels that are deep inside the body. MRI machines produce a magnetic flux density with a constant orientation, but our prototype contains a permanent magnet and actuation requires a rotating magnetic field. Ultrasound scanning gives a clear picture of soft tissues that do not show up well on X-ray images [22]. Additionally, ultrasonography does not generate ionizing radiation, removing the need for shielding and protective equipment.

3D medical ultrasound imagers are commercially available. Some systems use a 1D phased array transducer that moves and acquire multiple 2D images to generate 3D data [23], [24]. Other systems, such as the Imasonic 2D arrays (imasonic.com), use a 2D phased array transducer that acquires 3D information. Both methods achieve relatively low frame rates (60 acquisitions per second maximum [24]). In addition, 3D ultrasonography probes cost more than 2D probes. The robotic system presented in this paper uses an echocardiograph with a 1D phased array transducer to track a magnetic swimmer. This type of system can acquire 2D images at a rate of 1,000 fps. Adopting this system could facilitate and accelerate the development of medical magnetic robots by providing a sensing solution accessible to many research labs. Ultrasonography is more affordable than other medical imaging methods. An affordable system would also be accessible to more medical

However, the previous papers [16]—[21] did not describe how to perform closed-loop path following with only ultrasound feedback. To address this problem, this paper presents a control method that only uses 2D ultrasonography as a sensor to measure the swimmer's position and perform closed-loop path following. With this method, the swimmer is controlled in all three directions and stays in the ultrasound beam or within close proximity.

II. TRACKING A MAGNETIC SWIMMER USING ULTRASONOGRAPHY

A. System description

The magnetic manipulator used in this study was presented in [25] and is only briefly described in the present paper. It has six electromagnets (EMs) arranged in a cube shape. This EM configuration is not a Helmholtz coils system but a more general arrangement where the current in each EM is controlled independently and allows generating both magnetic field and gradient. The swimmer navigates inside a $150 \times 150 \times 150$ mm acrylic tank filled with tap water which has a density of 1000 Kg/m³ and a dynamic viscosity of 1E-3 Pa·s. The tank is placed at the center of the magnetic manipulator (see Fig. 2). Two Basler acA800 cameras view from the right and top sides of the manipulator. Cameras were used in this study to measure the swimmer's position with camera feedback, calibrate the position measured by the ultrasound, and monitor the path tracking error of the system.

The ultrasound system used in this study is a Verasonics 32 LE ultrasound system (verasonics.com/vantage-32-le) with a 64-element 1D phased array transducer. The system consists of data acquisition hardware connected to the host controller computer. The acquisition hardware includes electronic modules for multi-channel transmit waveform generation, analog receive signal amplification and filtering, digital signal processing, and scan sequencing. In addition, the host computer contains a MATLAB program that allows the user to send, receive and sequentially execute ultrasound events. During our tests, we did not detect any interference between the ultrasound device and the magnetic field.

A UR3 robot arm was used to statically hold the ultrasound transducer (see Fig. 2). The ultrasound transducer was pressed against the water tank and oriented such that the imaging plane coincided with the circular path plane described in Section III-B. The imaging plane of the ultrasound is parallel to the *xy*-plane of the workspace. The ultrasound beam depth is 142 mm, the elevation focus range is from 50 to 70 mm, and the slice thickness is approximately 7.5 mm. Ultrasound gel was placed between the tank and the transducer to reduce the acoustic impedance and wave reflection, producing a clearer image.

The final system consists of four computers. An industrial computer (IC-3173) is used to run LabVIEW programs to drive the magnetic swimmer with an external magnetic field. Another computer runs two MATLAB instances. One instance executes a MATLAB script for running the Verasonics Ultrasound system to capture the real-time imaging. The other instance is utilized to send the swimmer's position detected from the ultrasound imaging to the LabVIEW PC through TCP/IP. The other two computers are used for the robotic arm and as a programming interface for the IC-3173. All devices were connected to a router for the TCP/IP connection.

B. Ultrasound imaging modes for swimmer detection

Four ultrasound modes are commonly used in medical imaging: A-mode, B-mode, M-mode, and Doppler mode [26]. A-mode (Amplitude mode) is the simplest type of ultrasound

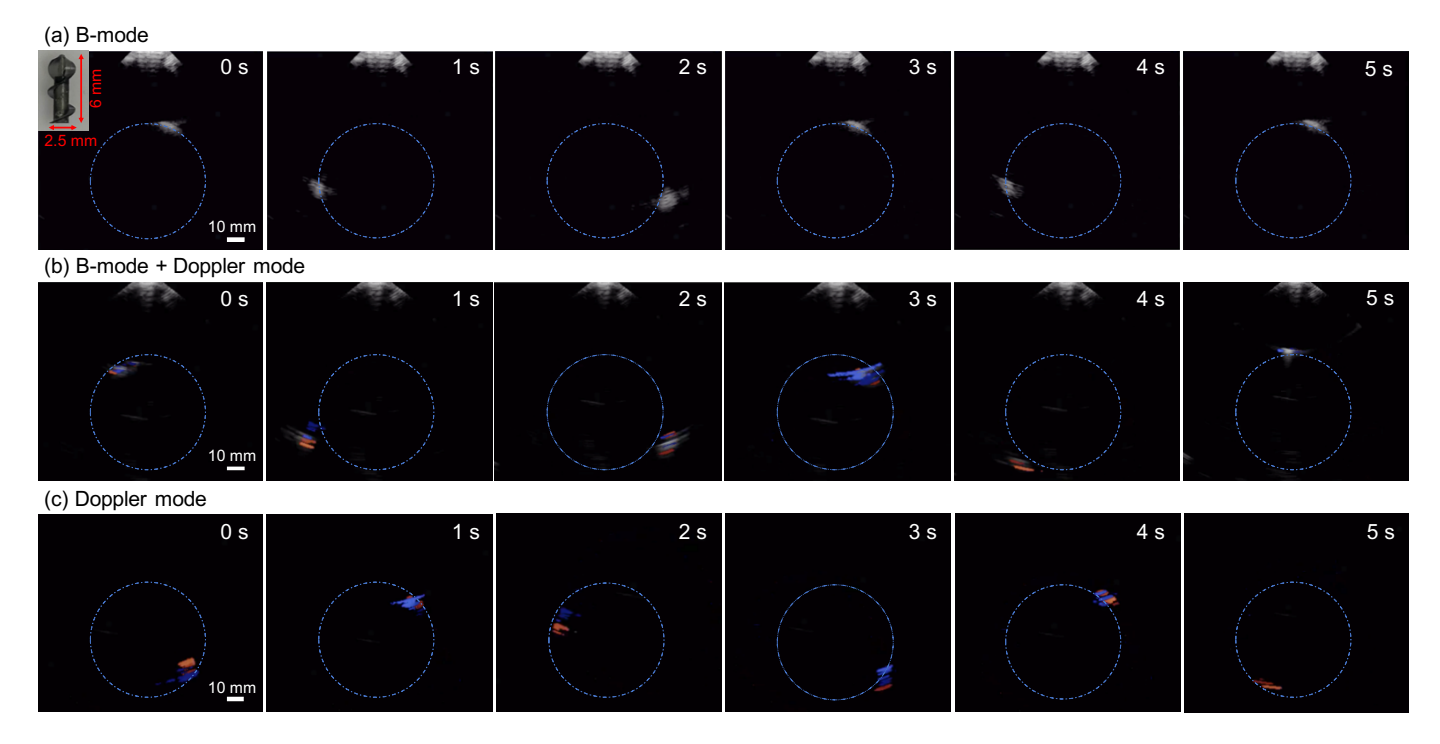


Fig. 3. Video snapshots of ultrasound images for tracking of the magnetic swimmer following a circular path under different ultrasound modes. The ultrasound imaging area is a subset of the square image. All pixels of the image that are not part of the imaging area are set to zero. The blue dashed-line circle indicates the circular path. Inset in the first picture is the swimmer used in the experiment. The video of this test is provided as multimedia material.

imaging mode. It uses a single sensor to scan a line through the object and displays the amplitude spikes as a function of depth. B-mode (Brightness mode) is the most common form of ultrasound imaging. Unlike A-mode, in B-mode, the transducer scans in the object's plane, and a 2D image is returned. The brightness of each pixel represents the amplitude or the intensity of the echo. M-mode (Motion mode) is a 1D image that is used for analyzing moving objects. For example, if the boundary of the object that produces the reflection moves relative to the probe, repeatedly measuring the distance of this object from the single transducer enables recording the amplitude and rate of motion in real-time. The Doppler mode uses the Doppler effect. Through this effect, ultrasonic waves interacting with moving objects experience a shift in their traveling frequency. The Doppler signal is extracted by quadrature demodulation technology and converted into a measure of the speed of the imaging object. This paper studies ultrasound B-mode and Doppler mode to track the swimmer because they produce 2D images.

Localizing the swimmer using ultrasound is split into three steps: (1) Find the best ultrasound imaging method to detect the swimmer. (2) Convert the position information from ultrasound imaging into workspace coordinates. (3) Use these coordinates (instead of camera coordinates) as feedback to perform closed-loop control. Camera feedback was used to stabilize the swimmer along a path to study the detection using ultrasonography.

Figure 3 shows ultrasound images taken while the magnetic swimmer followed a simple horizontal circular path using camera feedback under: B-mode, B-mode+Doppler mode, and Doppler mode. We adjusted the time gain compensation (TGC)

parameters to obtain better imaging resolution. TGC increases the received signal intensity with depth. The swimmer can be detected using ultrasound B-mode imaging as shown in Fig. 3(a), however the small size of the magnetic swimmer makes localization challenging. Figure (3) shows that adding the ultrasound Doppler mode based on the B-mode imaging increases the signal at the swimmer's position and makes the swimmer easier to distinguish from the surrounding environment. Doppler ultrasounds are only able to detect movements that are parallel to the ultrasound wave propagation direction. This characteristic does not impede the functioning of our system because the liquid movement around the swimmer has a component in each axis. The liquid rotates around the swimmer, toward its aft end and has a radial component behind it making detection in any orientation possible, even when the swimmer hovers without moving. The signal strength as well as the sign of the flow detected depends on the orientation of the swimmer with respect to the ultrasound beam. Also, the Doppler mode has adjustable sensitivity, and its various modes (e.g., color, power, velocity, and pulse wave) can be tuned to get higher imaging quality. Figure 3(c) shows ultrasound imaging results with only Doppler mode. By tuning the ultrasound imaging parameters to have a low false positive rate, our swimmer can be reliably detected. B-mode images could be used together with Doppler mode to locate the swimmer. We did not choose this solution as it would require a method to combine both images, increasing the computation duration and the complexity of the system. Doppler mode offers a higher signal-to-noise ratio than B-mode, so we chose to use only Doppler mode to locate the swimmer in all the remaining experiments of this paper.

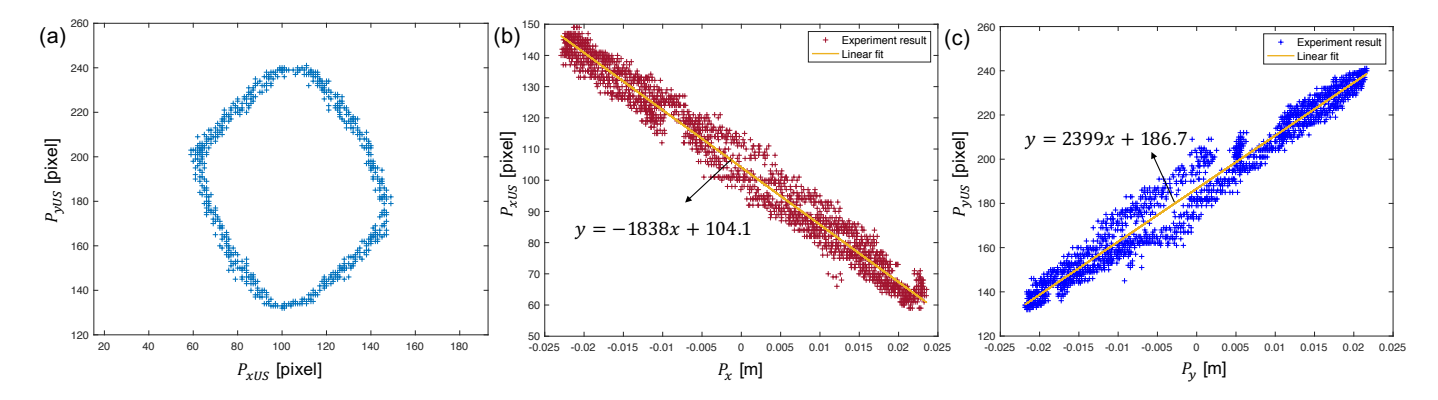


Fig. 4. a Experimental data of detecting the swimmer using ultrasound Doppler mode (5,482 data points). b and c show that the swimmer's position detected using both ultrasound Doppler imaging (P_{xUS}, P_{yUS}) and cameras (P_x, P_y) is linearly correlated. In these plots the swimmer was controlled using camera

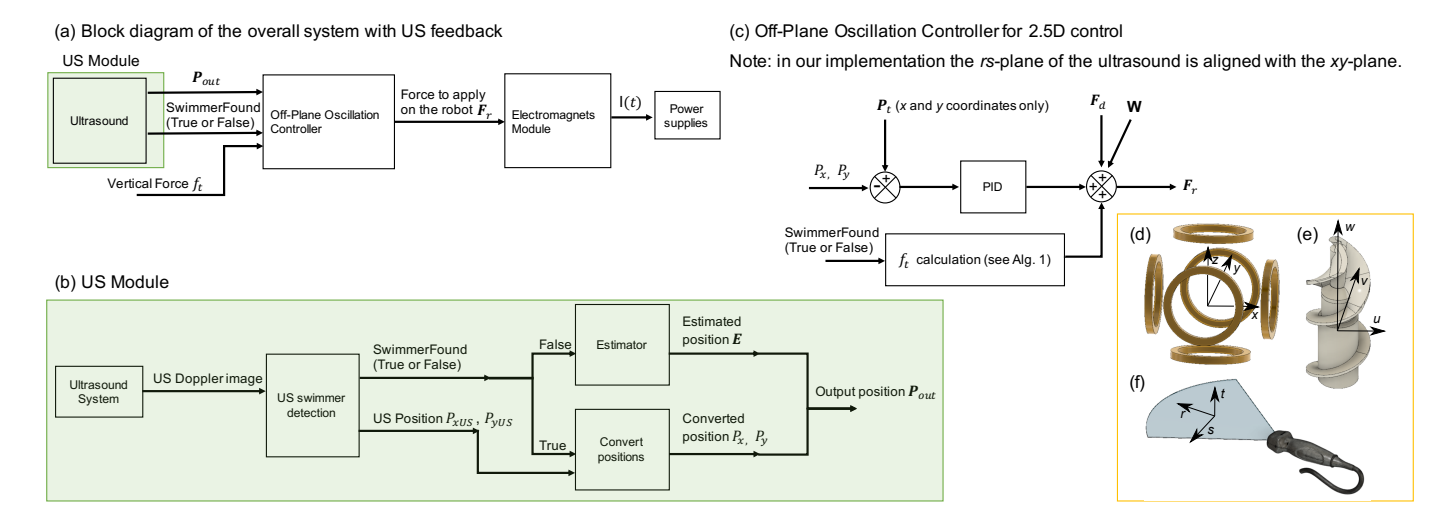


Fig. 5. Block diagram presenting the structure for 2.5D closed-loop path following using only ultrasound feedback. Inset: Schematic representation of the Cartesian reference frames used in this study. (d) Reference frame linked to the electromagnets. (e) Reference frame linked to the swimmer. (f) Reference frame linked to the ultrasound beam; the t axis is perpendicular to the image plane.

C. Ultrasound calibration

Calculating the position requires defining the relationship between the position measured from the ultrasound detection (P_{xUS}, P_{yUS}) and the position measured by the cameras (P_x, P_yUS) P_y). We recorded $(P_{xUS}, P_{yUS}, P_x, P_y)$ while the swimmer followed a 20 mm radius circular path. In this test, the rotational speed is constant at 50 Hz and the magnitude of the force is not controlled. The controller module in this test only changes the orientation of the rotating field to make the swimmer follow the circular path. Figure $\frac{4}{9}$ (a) shows experimental data locating the swimmer by finding the maximum intensity pixel using ultrasound Doppler mode. The circle path is distorted under ultrasound detection. Two major causes of distortion are (1) the physical structure of the probe and (2) medium changes. Transitions between different mediums causes refraction. Due to refraction, the part of the ultrasound wave that compresses the object passes through it faster than the part of the wave that decompresses it. As a result, the ultrasound image becomes geometrically distorted [27]. Figure [4](b) and (c) show that the swimmer's (x, y) positions measured with ultrasound Doppler mode and cameras are linearly correlated with coefficients of correlation equal to (0.9745, 0.9693). A higher order

polynomial fit could modestly improve the calibration, but at the expense of a more complicated calibration setup and more opaque equations. Therefore, the swimmer's position in the workspace was calculated using the following linear equations:

$$P_x = -\frac{P_{x\text{US}} - 104.1}{1838}$$

$$P_y = \frac{P_{y\text{US}} - 186.7}{2399}.$$
(1)

$$P_y = \frac{P_{yUS} - 186.7}{2399}. (2)$$

The calibration result depends on the size of the ultrasound image and the orientation and position of the ultrasound probe with respect to the frame of the magnetic manipulator. In the present study, we considered that only these parameters affect the calibration. In reality, the presence of materials with different acoustic impedance in the workspace may cause minor distortions. This effect was considered negligible in this paper.

III. 2.5D PATH FOLLOWING WITH ONLY ULTRASOUND **FEEDBACK**

A. System description

Figure 5(a) shows the block diagram for closed-loop path following using only ultrasound feedback. The system consists of three modules: the US module, the off-plane oscillation controller module, and the electromagnets module. We use the US module instead of the camera module to provide the swimmer's position information.

Figure 5(b) shows the detail of the US module. After receiving the ultrasound Doppler imaging from the ultrasound system, a MATLAB program calculates the swimmer's position and returns a Boolean value indicating if the swimmer is detected or not (SwimmerFound). If the swimmer is detected, the program calculates the position of the swimmer from ultrasound imaging (P_{xUS} , P_{yUS}) using (1) and (2). If the swimmer is not detected, we use a simplified estimation model to predict the swimmer's position given the previous position P'. The model was defined as:

$$\hat{P}_x = P_x' + k_p \cdot \omega_x \tag{3}$$

$$\hat{P}_y = P_y' + k_p \cdot \omega_y,\tag{4}$$

where ω is the rotational speed vector that defines the swimmer's rotational speed and orientation. k_p is a parameter that we tuned manually by trying multiple values, observing the results and selecting the one producing the best performance. P'_x and P'_y are the previous position and \hat{P}_x and \hat{P}_y are the estimated position. A Kalman filter could increase the performance of the system by modeling the effects of process and observation noises. Our implementation instead makes the assumption that the measurement of the swimmer position is accurate. The ultrasound only images a 2D slice of the workspace. To enable following a 2D path embedded in a 3D workspace, we implemented a new algorithm (see Section $\overline{\text{III-B}}$) that adds an additional force (f_t) that prevents the swimmer from leaving the ultrasound beam proximity.

B. Off-Plane Oscillation Controller

The 3D control of a magnetic swimmer using a 2D echocar-diography device as a position sensor is a challenging problem to solve because the sensor provides proportional feedback on just two axes (r and s axis), see Fig. 5 bottom right). Only binary information is available on the third axis (t axis), i.e., the presence or not of the swimmer within the ultrasound beam. We propose a new algorithm that uses this limited information to trap the swimmer within the ultrasound beam and its close proximity. With this algorithm, which we call the Off-Plane Oscillation Controller (OPOC), the swimmer tracks the path centerline in the r and s axis using a PID controller (see Fig. 5(c)) and oscillates in the t axis around the ultrasound beam. Thus, the swimmer is alternatively visible and invisible on the sensor.

Our system uses a basic model to control the swimmer in the absence of position feedback. Without measurement, the swimmer slowly drifts away from the path centerline due to the system uncertainty. The proposed controller generates a control command that makes the swimmer move within the t axis at a velocity V_{tc} in the absence of perturbations. If V_{tc} is greater than the system's velocity uncertainty in this axis, the swimmer moves in the direction requested by the controller. The swimmer can be stabilized within the ultrasound beam by simply multiplying V_{tc} by -1 when the swimmer leaves the

ultrasound beam, i.e., when the swimmer cannot be detected anymore in the ultrasound image. Preliminary experimental tests indicated that our ultrasound detection system could be tuned to avoid false positive detections of the swimmer. However, many false negative detections are produced. Therefore, we added a simple filter to our algorithm (see Alg. T).

```
Algorithm 1: CALCULATION OF f_t
 n \leftarrow 20;
                // filter length: number of
  detections needed to reverse direction.
 nNotFound \leftarrow n; // initialize variable to store
  the number of times steps since the last
  swimmer detection.
 f_t \leftarrow 1 ; // swimmer starts in the negative side
  of the t axis and needs to start with a
  positive force to cross the US beam
 Loop
    SwimmerFound ← USDETECTION(); // Measure
     using the ultrasonography device. True if
     the swimmer is detected.
    if SwimmerFound then
        nNotFound \leftarrow 0;
    else
        nNotFound \leftarrow nNotFound +1;
        if nNotFound == n then
           f_t = -f_t ; // change the direction of
            the force
        end
    end
 EndLoop
```

The performance of the OPOC can better be studied by introducing an adimensional variable $K = W_{US}/(|V_{tc}| \cdot \Delta T)$, where $W_{\rm US}$ is the thickness of the ultrasound beam and ΔT is controller time step. The normalized position of the swimmer along the t axis is $\hat{t_s} = t_s/W_{\rm US}$, where t_s is the position of the swimmer along the t axis. With these definitions, at each time step the swimmer moves along the t axis by a relative distance $d_s = 1/K$. The normalized width of the ultrasound beam is equal to 1. The OPOC algorithm was implemented in MATLAB and many simulations were performed to study its reliability. At the beginning of each simulation, t_s is randomly set between -1 and -0.5 with a uniform probability distribution. At each time step, the new position and direction of the swimmer are computed. The simulator randomly generates false negative detections with a probability P_n . The simulation is computed until the failure of the OPOC is detected. The OPOC failure is detected when \hat{t}_s has exited the ultrasound beam for more than n+1 time steps because, at this point, the swimmer will never return.

Simulations were performed for different values of P_n , K and n. 1,000 simulations were made for each parameter set and the average number of time steps before failure (n_{ts}) is presented in Fig. 6. As expected, simulations results show that decreasing P_n increases n_{ts} . Increasing K also increases n_{ts} . This is also an expected result because with a higher K value the system has more opportunities to detect the swimmer. K can be increased by increasing the ultrasound

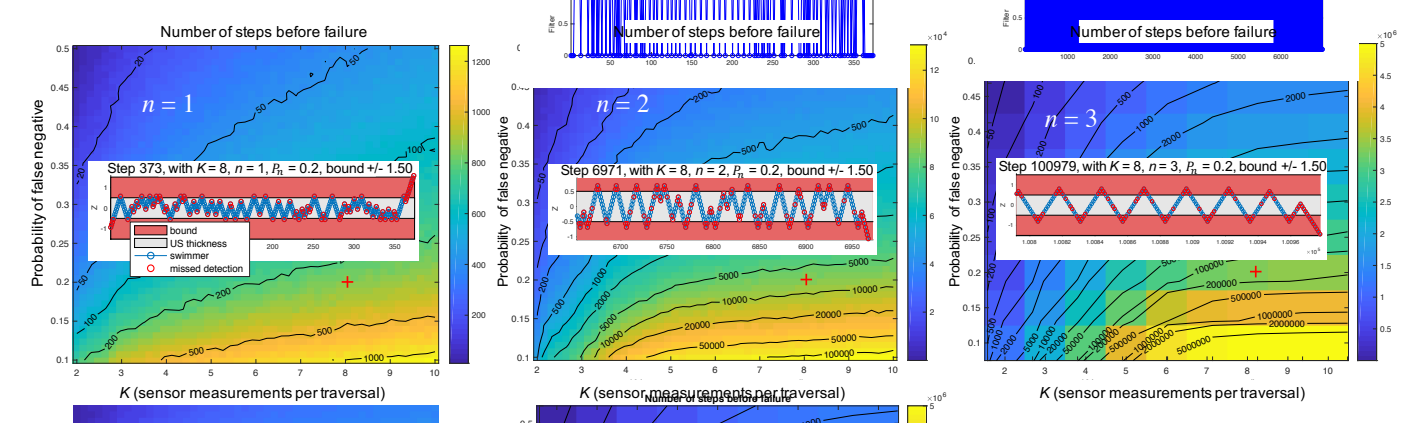


Fig. 6. These plots compare the affect of increasing the filter length. n is the filter length. K is an dimensionless constant that represents the number of times a swimmer can be imaged while it swims perpendicularly through the US imaging plane. The insets show representative swimmer paths at + signs.

image acquisition rate. Simulations were performed for n=1, 2 and 3. Increasing n increases the reliability of the system. The highest n_{ts} value obtained with our simulations is equal to 1.46×10^7 iterations. This corresponds to an average navigation duration of 406 hours before failure if we assume a time step of 0.1 s. With our simulation method, the computation time increases when the reliability of the system is increased. We did not perform simulations for n values larger than three because, with our implementation, the computation time was excessively long.

To fail, the swimmer must escape the US beam and never return. One way for this to happen is for the swimmer not to be detected as it passes through the sensing window (K successive false negatives). Another way is for the swimmer to be detected and then have n false negatives to switch direction followed immediately by sufficient false negatives to escape (at least 2n successive false negatives). This second type of failure is most common, starting with detection as the swimmer enters the boundary followed by 2n false detections. The representative swimmer paths for n=1 and n=2 in Fig. 6 show this type of failure, but the plot for n=3 moves two steps into the US beam before the string of seven false negatives.

IV. EXPERIMENTAL RESULTS

The controller was tested experimentally by performing a 2.5D path following of a racetrack path using only ultrasound feedback. A racetrack path was chosen because it is more challenging to follow than a circular path, as it contains straight sections and turns. The racetrack path has 40 mm straightaways and 45 mm diameter curves. The value of n=20 was used. The algorithm is simple, yet robust. In one experiment, we ran Alg. I for 16 minutes using only ultrasound feedback and the swimmer remained stable. Figure 8(a) shows a 3D view from a representative subset of the experimental results. 3000 data points are shown and the additional vertical force (f_t) changed 45 times. The top view plot shows that the swimmer follows the racetrack path. Figure 8(c) shows the side view with 600 data points colorcoded with respect to time. The swimmer changed z direction each time it passed the ultrasound imaging plane $(P_z = 0)$. Figure $\mathbb{S}(d)$ shows the swimmer's position detected using ultrasound Doppler mode. The swimmer's velocity magnitude along the z axis was calculated from this experimental data and was found to vary between 4.46 and 6.39 mm/s which represent a system uncertainty of 0.96 mm/s. During these tests, the K value was approximately equal to 72 (this value varies slightly during the navigation due to small variations of V_{tc} caused by the system's uncertainty). P_n appears to vary depending on the position along the path. We estimate the value of P_n to be between 0.2 and 0.35.

In the experiment, the RMS path tracking error was $8.12 \pm$ $2.88 \text{ mm} \ (2.98 \pm 2.09 \text{ mm} \text{ about the } x \text{ axis}, 5.32 \pm 3.51 \text{ mm}$ about the y axis, and 3.65 ± 2.64 mm about the z axis, along which the off-plane oscillations are performed. This result is worse than the performance using two cameras following the same racetrack centerline, with an average tracking error of 2.23 ± 0.55 mm (see Fig. 7). In body lengths, this corresponds to 1.35 ± 0.48 error with ultrasound and 0.37 ± 0.09 error with camera. The oscillation controller that is used with ultrasound feedback increases the tracking error along all axes because the oscillations of the swimmer produce temporary losses of position feedback when the swimmer is above or below the ultrasound beam. The performance of the system could be improved in the future. Currently, the position acquisition rate is equal to 219.2 ± 141.9 Hz. The swimmer detection algorithm is rudimentary but sufficient to make our system perform well. It is fast to compute (0.32 ms average with a standard deviation of 0.17 ms). Our ultrasound hardware alone can reach 1,000 fps. The position acquisition frequency is limited by the computer network. In our system, the position information is transferred to the NI-IC3173 via a TCP-IP connection using an ethernet router. This router is connected to four computers and the internet. The large variability of the data acquisition rate is due to the network latency which depends on the ongoing traffic.

V. CONCLUSION

This paper experimentally demonstrated for the first time that a 2D ultrasonography device is a sufficient sensor to perform 2.5D path following control of a rotating magnetic swimmer. We investigate the use of a new algorithm, the

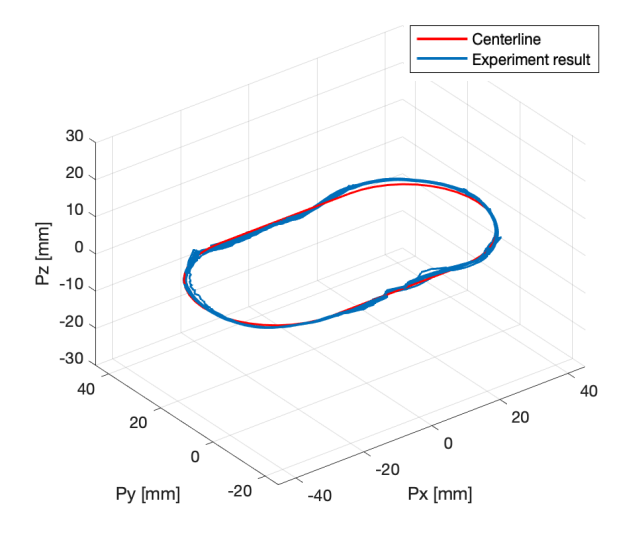


Fig. 7. Experimental result of the magnetic swimmer following a racetrack path has 40 mm straightaways and 45 mm diameter curves with camera feedback (3000 points are shown). The average error is 2.23 ± 0.55 mm.

off-plane oscillation controller, to allow stabilizing the swimmer within the ultrasound imaging plane. The swimmer was controlled in all three directions to follow a planar path. A theoretical study shows that the stability is affected by the probability of false negative detection as well as by an dimensionless number K that represents the number of times the swimmer could be detected while crossing the ultrasound beam. Simulations showed that this algorithm could trap the swimmer within the ultrasound beam for hours; however, it always eventually loses control because the system is not observable along the t axis. In the future, when such a loss of control happens, the system could execute a recovery strategy. The robotic arm could move the ultrasound probe to find the swimmer by scanning the workspace. Once the swimmer is located the system could resume path following.

A promising application for millimeter-scale rotating swimmers is the removal of pulmonary embolisms [13]. The swimmer will most likely be inserted inside a femoral artery and navigate through the aorta, the heart, and finally, the pulmonary arteries [11]. Blood flow velocity peaks on average at a value of 920 mm/s in the aorta and 630 mm/s in the pulmonary arteries [28] which is larger than the maximum velocity of our swimmer. However, the blood velocity varies in space [29] and time. Researchers have measured the realtime blood velocity in the ascending aorta using real-time MRI in [30]. Results show that the blood velocity quickly decreases after the heartbeat, down to less than 15% of the peak value. On average, the ascending aorta has a maximum diameter of 32.6 mm, and the pulmonary artery has a maximum diameter of 25.1 mm [31]. The blood velocity is maximum at the center of a vessel and equal to zero at the interface with the vessel wall. A path planner could exploit these variations of blood flow velocity to make progress moving against the blood flow. This type of algorithm could take into account the pulsation of the blood flow to position the swimmer close to the wall of the vessel when the blood velocity reaches high values. A swimmer able to navigate within blood vessels without touching the walls would be ideal; however, part of the

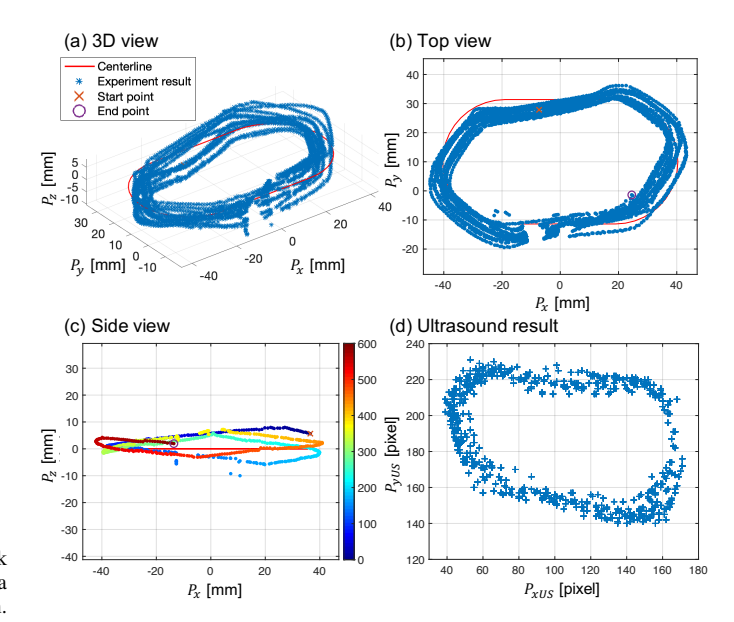


Fig. 8. Plot of path following by the swimmer using only ultrasound feedback (3000 points are shown, total rising time is 32 s, and sinking time is 28 s). **a** and **b** shows the 3D view and top view of the swimmer's position recorded by two cameras. The cameras were only used for recording the position, and never for control. **c** shows a side view with 600 data points color-coded by time. **d** shows the swimmer's position detected from the ultrasound imaging. See the attachment for a video of this experiment.

navigation will happen within blood vessels with a diameter smaller than the error obtained with our system. This will inevitably result in collisions with the walls of the arteries. But, magnetic swimmers are compliant systems. The force that they are able to generate is limited by the characteristics of the magnetic manipulator. They can remove blood clots by transferring mechanical energy over a long period (a few minutes [12]). As a result, we do not expect them to damage blood vessels significantly via short contacts; however, this must be verified experimentally in future work.

Future work will also study performance and stability of the system when performing position keeping and when following more tortuous paths. The proximity of an artery wall affects rotating swimmers [32], [33]. A more advanced controller that takes this effect into account needs to be studied. Such a controller could, for example, estimate the force produced by the swimmer-wall interaction and add a compensating component to the force applied to the swimmer (see Fig. 5). The control method presented in this paper could also be extended to enable 3D paths and make the method more robust by using a robot arm to move the ultrasound transducer. Future work preceding in-vivo experiments should also test the system within organ phantoms and in the presence of fluid flow.

REFERENCES

- N. Siauve, R. Scorretti, N. Burais, L. Nicolas, and A. Nicolas, "Electromagnetic fields and human body: a new challenge for the electromagnetic field computation," COMPEL-The international journal for computation and mathematics in electrical and electronic engineering, 2003
- [2] J. W. Martin, B. Scaglioni, J. C. Norton, V. Subramanian, A. Arezzo, K. L. Obstein, and P. Valdastri, "Enabling the future of colonoscopy with

TABLE I LIST OF VARIABLES USED IN THIS PAPER

Variable	Description	Unit	Size
W	Swimmer weight	N	3x1
\boldsymbol{F}_d	Drag force setpoint	N	3x1
ω	Swimmer rotation vector	$rad \cdot s^{-1}$	3x1
$oldsymbol{P}_{ ext{out}}$	Position calculated by the	m	2x1
	ultrasound module		
f_t	Force to apply to the swimmer	N	1x1
	along the t axis		
V_{tc}	Velocity of the swimmer	$\text{m}\cdot\text{s}^{-1}$	1x1
	along the z axis		
P_{x US	Swimmer x position	pixel	1x1
	measured via ultrasound		
$P_{y_{ m US}}$	Swimmer y position	pixel	1x1
	measured via ultrasound		
P_x	Swimmer x position in the workspace, y and z similar	m	1x1
$oldsymbol{E}$	Estimated swimmer position	m	3x1
P_n	Probability of false negative		JAI
	detection	Dimensionless	1x1
n	Filter length used by the OPOC	Dimensionless	1x1
K	Calculated dimensionless variable	Dimensionless	1x1
$W_{ m US}$	Thickness of the ultrasound beam	m	1x1
ΔT	Controller time step	S	1x1
$\widehat{t_s}$	Normalized swimmer position	Dimensionless	1x1
	along the t axis		
t_s	Position of the swimmer	m	1x1
	along the t axis		
$\widehat{d_s}$	Normalized distance traveled by	Dimensionless	1x1
	the swimmer during each time step		
n_{ts}	Average number of iterations	Dimensionless	1x1
	before failure of the OPOC		

- intelligent and autonomous magnetic manipulation," *Nature machine intelligence*, vol. 2, no. 10, pp. 595–606, 2020.
- [3] S. H. Kim and K. Ishiyama, "Magnetic robot and manipulation for active-locomotion with targeted drug release," *IEEE/ASME Transactions* On Mechatronics, vol. 19, no. 5, pp. 1651–1659, 2013.
- [4] T. Xu, J. Zhang, M. Salehizadeh, O. Onaizah, and E. Diller, "Millimeter-scale flexible robots with programmable three-dimensional magnetization and motions," *Science Robotics*, vol. 4, no. 29, 2019.
- [5] X. Wu, J. Liu, C. Huang, M. Su, and T. Xu, "3-d path following of helical microswimmers with an adaptive orientation compensation model," *IEEE Transactions on Automation Science and Engineering*, vol. 17, no. 2, pp. 823–832, 2019.
- [6] T. Xu, G. Hwang, N. Andreff, and S. Régnier, "Planar path following of 3-d steering scaled-up helical microswimmers," *IEEE Transactions* on Robotics, vol. 31, no. 1, pp. 117–127, 2015.
- [7] M. Koleoso, X. Feng, Y. Xue, Q. Li, T. Munshi, and X. Chen, "Micro/nano-scale magnetic robots for biomedical applications," *Materials Today Bio*, p. 100085, 2020.
- [8] E. E. Niedert, C. Bi, G. Adam, E. Lambert, L. Solorio, C. J. Goergen, and D. J. Cappelleri, "A tumbling magnetic microrobot system for biomedical applications," *Micromachines*, vol. 11, no. 9, p. 861, 2020.
- [9] I. S. Khalil, A. Adel, D. Mahdy, M. M. Micheal, M. Mansour, N. Hamdi, and S. Misra, "Magnetic localization and control of helical robots for clearing superficial blood clots," *APL bioengineering*, vol. 3, no. 2, p. 026104, 2019.
- [10] U. Bozuyuk, O. Yasa, I. C. Yasa, H. Ceylan, S. Kizilel, and M. Sitti, "Light-triggered drug release from 3d-printed magnetic chitosan microswimmers," ACS nano, vol. 12, no. 9, pp. 9617–9625, 2018.
- [11] J. Leclerc, H. Zhao, D. Z. Bao, A. T. Becker, M. Ghosn, and D. J. Shah, "Agile 3d-navigation of a helical magnetic swimmer," in 2020 IEEE International Conference on Robotics and Automation (ICRA). IEEE, 2020, pp. 7638–7644.
- [12] J. Leclerc, H. Zhao, D. Bao, and A. T. Becker, "In vitro design investigation of a rotating helical magnetic swimmer for combined 3d navigation and blood clot removal," *IEEE Transactions on Robotics*, vol. 36, no. 3, pp. 975–982, 2020.
- [13] J. Leclerc, Y. Lu, A. T. Becker, M. Ghosn, and D. J. Shah, "Resonating magnetic manipulation for 3d path-following and blood clot removal using a rotating swimmer," in 2020 IEEE/RSJ International Conference on Intelligent Robots and Systems (IROS). IEEE, 2020, pp. 3083–3090.

- [14] A. Aziz, S. Pane, V. Iacovacci, N. Koukourakis, J. Czarske, A. Menciassi, M. Medina-Sánchez, and O. G. Schmidt, "Medical imaging of microrobots: Toward in vivo applications," ACS nano, vol. 14, no. 9, pp. 10 865–10 893, 2020.
- [15] Q. Wang, L. Yang, J. Yu, P. W. Y. Chiu, Y.-P. Zheng, and L. Zhang, "Real-time magnetic navigation of a rotating colloidal microswarm under ultrasound guidance," *IEEE Transactions on Biomedical Engi*neering, vol. 67, no. 12, pp. 3403–3412, 2020.
- [16] Q. Wang, K. F. Chan, K. Schweizer, X. Du, D. Jin, S. C. H. Yu, B. J. Nelson, and L. Zhang, "Ultrasound doppler-guided real-time navigation of a magnetic microswarm for active endovascular delivery," *Science Advances*, vol. 7, no. 9, p. eabe5914, 2021.
- [17] Z. Yang, L. Yang, M. Zhang, Q. Wang, S. C. H. Yu, and L. Zhang, "Magnetic control of a steerable guidewire under ultrasound guidance using mobile electromagnets," *IEEE Robotics and Automation Letters*, vol. 6, no. 2, pp. 1280–1287, 2021.
- [18] S. Pane, V. Iacovacci, E. Sinibaldi, and A. Menciassi, "Real-time imaging and tracking of microrobots in tissues using ultrasound phase analysis," *Applied Physics Letters*, vol. 118, no. 1, p. 014102, 2021.
- [19] Q. Wang and L. Zhang, "Ultrasound imaging and tracking of micro/nanorobots: From individual to collectives," *IEEE Open Journal of Nanotechnology*, vol. 1, pp. 6–17, 2020.
- [20] D. Mahdy, R. Reda, N. Hamdi, and I. S. Khalil, "Ultrasound-guided minimally invasive grinding for clearing blood clots: promises and challenges," *IEEE Instrumentation & Measurement Magazine*, vol. 21, no. 2, pp. 10–14, 2018.
- [21] I. S. Khalil, D. Mahdy, A. El Sharkawy, R. R. Moustafa, A. F. Tabak, M. E. Mitwally, S. Hesham, N. Hamdi, A. Klingner, A. Mohamed *et al.*, "Mechanical rubbing of blood clots using helical robots under ultrasound guidance," *IEEE Robotics and Automation Letters*, vol. 3, no. 2, pp. 1112–1119, 2018.
- [22] W. Zhang, I. Oraiqat, H. Lei, P. L. Carson, I. EI Naqa, and X. Wang, "Dual-modality x-ray-induced radiation acoustic and ultrasound imaging for real-time monitoring of radiotherapy," *BME Frontiers*, vol. 2020, 2020.
- [23] R. W. Prager, U. Z. Ijaz, A. Gee, and G. M. Treece, "Three-dimensional ultrasound imaging," *Proceedings of the Institution of Mechanical En*gineers, Part H: Journal of Engineering in Medicine, vol. 224, no. 2, pp. 193–223, 2010.
- [24] Q. Huang and Z. Zeng, "A review on real-time 3d ultrasound imaging technology," *BioMed research international*, vol. 2017, 2017.
- [25] J. Leclerc, B. Isichei, and A. T. Becker, "A magnetic manipulator cooled with liquid nitrogen," *IEEE Robotics and Automation Letters*, vol. 3, no. 4, pp. 4367–4374, 2018.
- [26] F. A. Duck, A. C. Baker, and H. C. Starritt, Ultrasound in medicine. CRC Press, 2020.
- [27] T. Bland, J. Tong, B. Ward, and N. Parker, "Geometric distortion of area in medical ultrasound images," in *Journal of Physics: Conference Series*, vol. 797, no. 1. IOP Publishing, 2017, p. 012002.
- [28] J. M. Gardin, C. S. Burn, W. J. Childs, and W. L. Henry, "Evaluation of blood flow velocity in the ascending aorta and main pulmonary artery of normal subjects by doppler echocardiography," *American heart journal*, vol. 107, no. 2, pp. 310–319, 1984.
- [29] J. Garcia, R. L. Van Der Palen, E. Bollache, K. Jarvis, M. J. Rose, A. J. Barker, J. D. Collins, J. C. Carr, J. Robinson, C. K. Rigsby et al., "Distribution of blood flow velocity in the normal aorta: effect of age and gender," *Journal of Magnetic Resonance Imaging*, vol. 47, no. 2, pp. 487–498, 2018.
- [30] A. Joseph, J. T. Kowallick, K.-D. Merboldt, D. Voit, S. Schaetz, S. Zhang, J. M. Sohns, J. Lotz, and J. Frahm, "Real-time flow mri of the aorta at a resolution of 40 msec," *Journal of Magnetic Resonance Imaging*, vol. 40, no. 1, pp. 206–213, 2014.
- [31] Q. A. Truong, J. M. Massaro, I. S. Rogers, A. A. Mahabadi, M. F. Kriegel, C. S. Fox, C. J. O'Donnell, and U. Hoffmann, "Reference values for normal pulmonary artery dimensions by noncontrast cardiac computed tomography: the framingham heart study," *Circulation: Cardiovascular Imaging*, vol. 5, no. 1, pp. 147–154, 2012.
- [32] H. O. Caldag, A. Acemoglu, and S. Yesilyurt, "Experimental characterization of helical swimming trajectories in circular channels," *Microfluidics and Nanofluidics*, vol. 21, no. 8, pp. 1–13, 2017.
- [33] A. Barbot, D. Decanini, and G. Hwang, "The rotation of microrobot simplifies 3d control inside microchannels," *Scientific reports*, vol. 8, no. 1, pp. 1–9, 2018.